Ocean Engineering 257 (2022) 111669

Contents lists available at ScienceDirect

Ocean Engineering

journal homepage: www.elsevier.com/locate/oceaneng

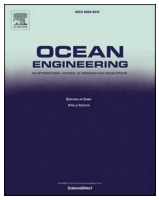

Data-driven modeling of wind waves in upper Delaware Bay with living shorelines

Nan Wang [a], Qin Chen [b,*], Ling Zhu [c], Hongqing Wang [d]

[a] Department of Civil and Environmental Engineering, Northeastern University, 400 SN, Boston, MA, 02115, USA
[b] Department of Civil and Environmental Engineering, Department of Marine and Environmental Sciences, Northeastern University, 471 SN, Boston, MA, 02115, USA
[c] Department of Civil and Environmental Engineering, Northeastern University, 400 SN, 360 Huntington Avenue, Boston, MA, 02115, USA
[d] U.S. Geological Survey, Wetland and Aquatic Research Center, Baton Rouge, LA, 70803, USA

ARTICLE INFO

Keywords:
Living shorelines
Constructed oyster reefs
Fully connected neural networks
Long short-term memory
Wave power reduction

ABSTRACT

Living shoreline projects have been built to preserve coastal ecosystems under future climate change and sea level rise. To quantify the wave power variation across living shorelines, the wave characteristics around the constructed oyster reefs (CORs) in upper Delaware Bay were investigated in this study. Wave parameters seaward and shoreward of CORs were recorded by wave gauges in early 2018. Four winter storms happened in this period and induced strong winds and coastal flooding at the study site. To estimate the wind wave characteristics across the CORs on a yearly basis, soft computing-based models combining fully connected neural networks and long short-term memory were developed to extend the two-month energetic wave measurements. The results show that when CORs were emergent or slightly submerged, the averaged wave height attenuation was about 39.8% from the offshore gauge to the nearshore gauge (behind CORs) during 2018–2020, owing to the combined effect of nearshore bathymetric changes and CORs. Furthermore, it was found that the annually averaged wave power reduction from offshore to nearshore at the study site was about 30.0% in 2018, 2019, and 2020. This study provides a novel framework to predict long-term wave characteristics based on short-term wave measurements using soft computing-based models.

1. Introduction

Delaware Bay and its river estuaries sustain one of the most populated regions and rich ecosystems in the world, providing nesting habitats for nearshore fish and shellfish communities (e.g., Baker et al., 2004; Wang et al., 2021). However, due to energetic waves and storm surges, Delaware Bay coastlines have suffered chronic erosion with an estimated rate ranging from about 0.1 to 1 m/yr (Kukulka et al., 2017). Recently, many living shoreline restoration projects have been developed along the Northeast and Mid-Atlantic coasts in the United States to restore and protect coastal ecosystems and mitigate the impact of sea level rise. Since the global sea level was estimated to increase from about 0.2 m to over 1.0 m by 2100 (e.g., Schwimmer, 2001; Kopp et al., 2014), Delaware Bay shorelines and salt marshes will become even more vulnerable. Therefore, an improved understanding of the effectiveness of living shoreline structures can help inform the success of future restoration projects.

Living shoreline projects have been constructed globally using various materials, such as freshwater plants, mangroves, and oyster reefs (Bayraktarov et al., 2016; Besse et al., 2018; Smith et al., 2020). Wiberg et al. (2019) monitored waves around the restored intertidal oyster reefs in the southern Delmarva Peninsula, USA, in July 2011, February 2012, July 2014, and May 2017. They found that the wave energy approaching the shoreline can be reduced by oyster reefs when the edge elevations are close to the mean sea level (MSL). In contrast, oyster reefs have a negligible impact on waves in deeper water, so reefs cannot protect marshes with high surface elevations. Zhu et al. (2020) conducted a field experiment to study variations in wave characteristics and wave spectra across constructed oyster reefs in a small cove in upper Delaware Bay from January 31 to April 2, 2018. They demonstrated that the wave power attenuation across living shorelines depends on several factors, such as the reef crest freeboard, the surrounding bathymetry, and the local wave environment. Overall, the success of living shoreline projects and the associated long-term (e.g., longer than one year) ecological benefits heavily rely on an accurate examination of wave power variation across the living shorelines, since the erosion rates are highly

* Corresponding author.
E-mail addresses: wang.nan@northeastern.edu (N. Wang), q.chen@northeastern.edu (Q. Chen), l.zhu@northeastern.edu (L. Zhu), wangh@usgs.gov (H. Wang).

https://doi.org/10.1016/j.oceaneng.2022.111669
Received 23 January 2022; Received in revised form 17 April 2022; Accepted 28 May 2022
Available online 6 June 2022

correlated with wave power (e.g., Schwimmer, 2001; Priestas et al., 2015; McLoughlin et al., 2015; Sanford and Gao, 2018; Everett et al., 2019).

Smith et al. (2020) provided a scoping review of living shoreline research and found that most projects only offered a short-term snapshot of performance with spatially and temporally limited in-situ measurements, such as Wiberg et al. (2019) and Zhu et al. (2020) mentioned above. However, long-term wave data are essential to thoroughly examine wave power changes across living shorelines. Since collecting such field measurements is usually costly, different models can be employed to simulate long-term wave conditions around living shorelines, such as numerical (e.g., Booij et al., 1999; Chen et al., 2000; Tolman, 1991) and soft computing-based wave models (e.g., Makarynskyy, 2006; Parker and Hill, 2017).

During the past several decades, considerable progress has been made in physics-based wave models based on wave action and momentum balance principles. Different wave models can be employed to simulate spatial and temporal characteristics of waves in shallow bays (e.g., Pareja-Roman et al., 2019; Chen et al., 2018; Mariotti et al., 2010; Salatin et al., 2021). For example, Kukulka et al. (2017) combined the Regional Ocean Modeling System (ROMS, Shchepetkin and McWilliams, 2005) and the spectral model of Simulating Waves Nearshore (SWAN, Booij et al., 1999) to investigate surface wave dynamics in Delaware Bay. They revealed that bathymetric refraction could shelter the bay from energetic swell waves originating from the open ocean. Similarly, Chen et al. (2018) coupled ROMS and SWAN to simulate waves in the Delaware Estuary. They found that during southerly wind conditions, wave energy is near equilibrium in the lower bay, and waves in the midestuary are attenuated by the combination of whitecapping and bottom friction. Mariotti et al. (2010) applied the numerical hydrodynamic model WWTM (Wind Wave Tidal Model, Carniello et al., 2011) to the lagoons of the Virginia Coast Reserve. They found that the storm surge could significantly influence the marsh edge erosion rate by increasing the lagoon water level. Although physics-based numerical models generally provide satisfactory results, direct application of these models to living shoreline projects can encounter some challenges. For instance, physics-based numerical models require a precise description of initial and boundary conditions to effectively capture the downstream wave and flow fields (Kissas et al., 2020). Thus, nested computational domains may be required to provide accurate boundary conditions, which are usually time-consuming to apply. Additionally, traditional wave models may involve the cumbersome generation of computational meshes for complicated geometries. By contrast, soft computing-based models can be used as surrogates to simulate wave responses to living shorelines without a high demand for computational resources.

Machine learning methods, such as artificial neural network (ANN), support vector machine (SVM), long short term memory (LSTM), Bayesian Network (BN), and decision trees (DT) have been widely adopted in soft computing-based models for simulating waves in the last several decades (e.g., Deo and Naidu, 1998; Deo et al., 2001; Cornejo-Bueno et al., 2016; Sadeghifar et al., 2017; Oh and Suh, 2018; Stringari et al., 2019; Zheng et al., 2020; Chen et al., 2021; Wei, 2021; Miky et al., 2021; Jörges et al., 2021; Elbisy and Elbisy, 2021; Bento et al., 2021; Mares-Nasarre et al., 2021; Lee et al., 2021; Wei and Davison, 2022). For example, James et al. (2018) used ANNs and SVMs to surrogate SWAN for predicting significant wave height (H_s) and characteristic wave period, respectively. Their model ran over 4,000 times faster than SWAN and exhibited a similar accuracy for wave prediction in the region of interest. Malekmohamadi et al. (2011) compared the performance of SVM, BN, ANN, and Adaptive Neuro FIS methods for mapping wind data to wave height in Lake Superior, USA, and found that all these methods, except BN, provided acceptable predictions for significant wave height, H_s. Wang et al. (2022) proposed a hybrid approach integrating the physics-based model with machine learning algorithms (i.e., BRT and ANN) to estimate wave parameters and identify sources of error in physics-based models (i.e., SWAN). Other machine learning applications include applying the LSTM for forecasts and reconstructions of H_s and wave power (Pirhooshyaran and Snyder, 2020), and using fuzzy systems to predict H_s and wave energy flux at one buoy location along the California Coast with observation data from nearby buoys as inputs (Cornejo-Bueno et al., 2016). These soft computing-based algorithms provide a new tool to solve wave prediction and classification problems in coastal and estuarine systems.

As mentioned above, most existing studies on wave responses to living shoreline structures focused on field measurements, which were relatively short in duration (i.e., days to months). To better investigate the wave power variation across the living shoreline structures, we proposed using soft computing-based methods to extend the short-term measurement for long-term analysis. To the best of the authors' knowledge, soft computing-based methods have not been applied to examine the wave height changes across living shoreline structures. The purpose of this study is twofold: (i) to develop a framework for investigating long-term wind wave characteristics based on short-term wave measurements with soft computing-based models, and (ii) to examine the wave power variation across the constructed oyster reefs (CORs) in upper Delaware Bay. A test of the data representativeness is proposed in the framework to examine whether the measured wave parameters in a short period can be used to predict long-term wave processes. This step is crucial to ensure that the predicted long-term wave characteristics are reliable (Section 2.3.2). Compared to physics-based numerical models, using soft computing-based models can significantly reduce the computation cost. Therefore, this framework can be applied as a surrogate to estimate long-term wave characteristics based on short-term wave measurements without a high demand for computational resources.

2. Methods

2.1. Study area

The construction of 3,000 ft (915 m) of living shorelines and breakwaters was carried out along the coastline between Money Island Marina and Gandys Beach in upper Delaware Bay in 2016. The project aimed to rebuild salt marshes and adjacent uplands ruined by Hurricane Sandy in 2012 and increase the resistance of shorelines to future storms and erosion (Wang et al., 2021). The location of our study site is at a small cove close to Money Island in upper Delaware Bay (Fig. 1). The CORs were built of prefabricated concrete blocks, with dimensions about 2.4–7 m long, 0.5–0.9 m wide, and 0.4–0.8 m tall, and the mean distance between neighboring CORs is 3.9 m (Fig. E1). Since the tides are predominantly semi-diurnal with a range exceeding 2 m at the study site, the CORs are submerged during high tides and completely exposed during low tides. More details of the geometry of the CORs and the reef setup can be found in Zhu et al. (2020) and Wang et al. (2021).

2.2. Wave measurements

Six bottom-mounted OSSI (Ocean Sensor Systems Inc) wave gauges (WG) were deployed on Gandys Beach from January 31 to April 2, 2018 (Fig. 1). The wave gauges were set to record a burst of 20-min every 30 min (i.e., 48 bursts per day) with a sampling frequency of 10 Hz, so that short wind waves could be resolved with a high sampling frequency

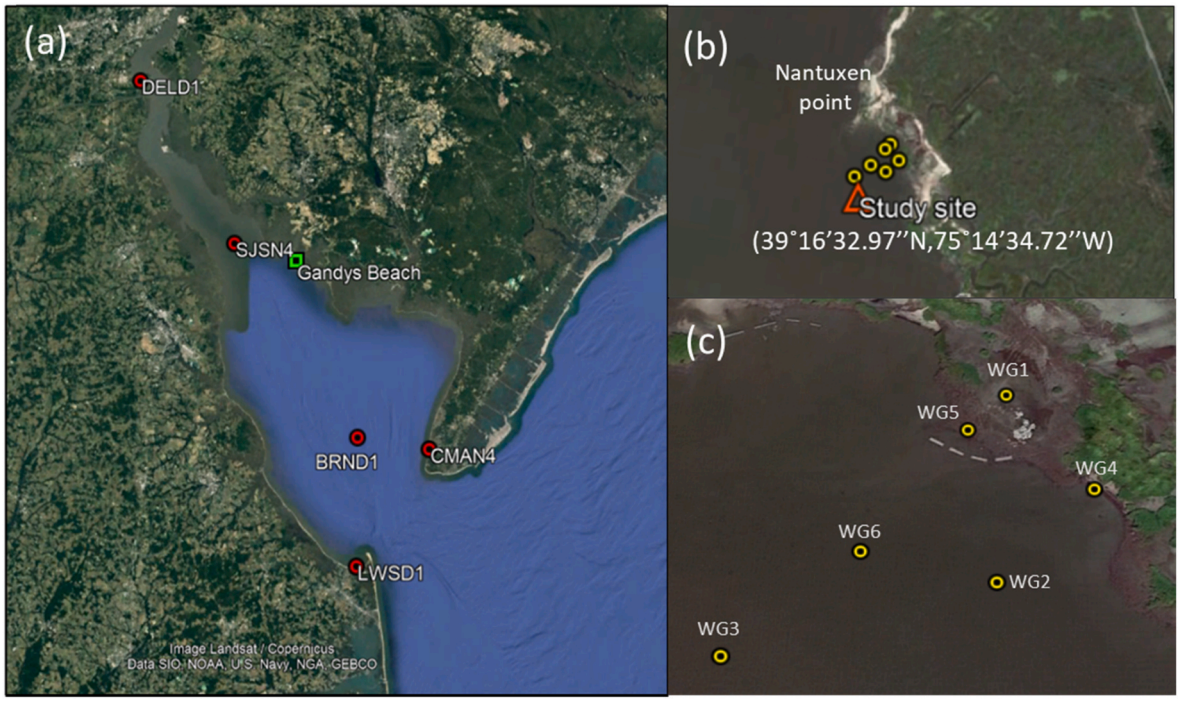

Fig. 1. (a) A map showing the study area (green dot, i.e., Gandys Beach) and nearby NOAA wind stations (red dots) in Delaware Bay. (b) A map showing the location of the wave gauges (yellow dots) and the shoreline of the study area. (c) A map showing the locations of wave gauges with the locations of the CORs represented by the dashed lines. (For interpretation of the references to color in this figure legend, the reader is referred to the Web version of this article.)

during this study period. To investigate the wave height variation across the living shorelines, we focused on the wave characteristics at WG3, WG6, WG5, and WG1 in this study, because they were deployed along a transect that crosses the CORs.

The data processing and analysis applied to the raw time series pressure data closely followed the methods outlined in Karimpour and Chen (2016). The raw pressure data were first converted to water depth, and then a wave spectral analysis was performed to extract the relevant wave parameters. The Ocean Wave Analyzing Toolbox (Oceanlyz v1.4) was employed for the wave spectral analysis (Karimpour and Chen, 2017; Wang et al., 2020). Generally, the marsh edge erosion is attributed to both remotely generated swell waves and locally generated wind waves. However, it was found that swell energy remains nearly unchanged on the seaward and shoreward sides of CORs (Zhu et al., 2020; Wang et al., 2021). Moreover, since energetic wave conditions are characterized by wind-driven seas at the study site (e.g., Kukulka et al., 2017; Chen et al., 2018), we only considered the influence of sea waves in this study. It is worth mentioning that the proposed framework can also be used to predict the swell waves with some adjustments. More details can be found in Section 4.2.

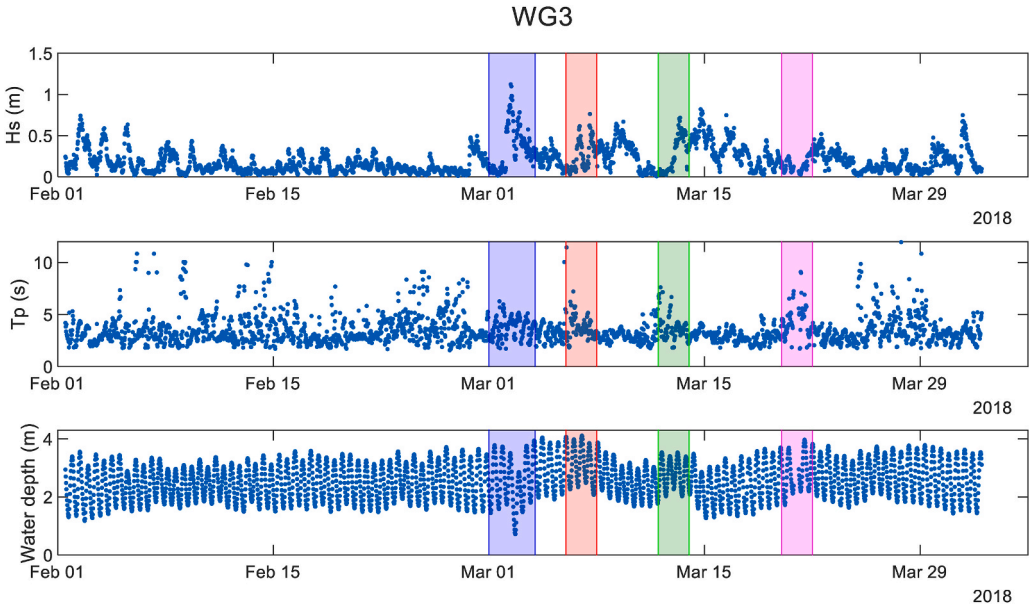

Fig. 2. The measured significant wave height, peak wave period, and local water depth at WG3 from January 31 to April 2, 2018 (wind sea only). The shaded areas represent the four nor'easters in March 2018: Riley, Quinn, Skylar, and Toby.

The method in Hwang et al. (2012) was employed to separate sea and swell energies. Given that T_p from Oceanlyz v1.4 can be miscalculated when H_s is small, small waves with $H_s < 7$ cm were removed from the rest of the analysis. Fig. 2 shows an example of wave parameters and water depth measured at WG3. Four nor'easters happened during the two months of 2018 (i.e., Riley on March 2, Quinn on March 7, Skylar on March 14, and Toby on March 21) and induced strong winds, large precipitation, and coastal flooding to the study site, providing an informative dataset to design soft-computing based models for predicting wind wave parameters. The feasibility of employing the developed models to estimate wave parameters around CORs throughout the years was further examined in Section 2.3.2.

2.3. Data-driven models

In this study, the wave measurements are available for two months in 2018 (i.e., from January 31 to April 2, 2018). To estimate wave fields around the CORs over a longer period (e.g., yearly), artificial neural networks (ANN) were designed to study nonlinear and complex relationships between wave parameters and forcing functions based on the 2-month measurements. Specifically, we developed four composite ANNs to predict wind wave characteristics at each wave gauge location (i.e., WG3, WG6, WG5, and WG1) in 2015, 2016, 2018, 2019, and 2020. Since CORs have not been constructed until the summer of 2016, the simulated wave field behind CORs (i.e., WG1 and WG5) was unreal in 2015 and 2016. The composite networks were designed based on prior knowledge of wave responses to forcing functions and the relationship between wave parameters. Specifically, the wind and water depth data were selected as input features to estimate wind seas at the study site over the years, because both of them are critical for predicting wind waves in a shallow estuary (Karimpour and Chen, 2017). More details about the inputs and network structures can be found in Sections 2.3.3 and 2.3.4.

It should be noted that a representative test is required to examine whether the measured wave parameters during the two months can be used for studying long-term wave fields (Section 2.3.2). This step aims at ensuring that the predicted long-term wave characteristics are reasonable because ANNs cannot do extrapolation (Willard et al., 2020). The methods applied to determine winds and wave fields at the study site are shown in the following subsections, providing a framework to investigate long-term wind wave characteristics based on short-term wave measurements using soft computing-based models.

2.3.1. Spatial variation of winds in Delaware Bay

To study the wave height variation across the CORs, the wind field in Delaware Bay was examined first because the wind is the main driving force of wind seas. Due to the variability in estuarine wind fields (Mariotti et al., 2018), the wind data from meteorological stations scattered throughout Delaware Bay were used to analyze wind sea characteristics at the study site. As a result, the wind data from five NOAA (National Oceanic and Atmospheric Administration) stations at DELD1, SJSN4, BRND1, LWSD1, and CMAN4 were collected (Fig. 1). The wind roses in 2015 and 2016 manifest the significant spatial

Table 1
Wind data availability at DELD1, SJSN4, BRND1, LWSD1, and CMAN4. Numbers represent the months when wind data are available.

NOAA stations	2015	2016	2018	2019	2020
8551762 DELD1	1–12	1–12	1–12	1–12	1–10
8537121 SJSN4	1–12	1–12	1, 8-12	1-5, 9-12	1–6
8555889 BRND1	1–12	1–12	1–11	–	1–10
8557380 LWSD1	1–12	1–12	1–12	1–12	1–10
8536110 CMAN4	1–12	1–12	1–12	1–12	1–10

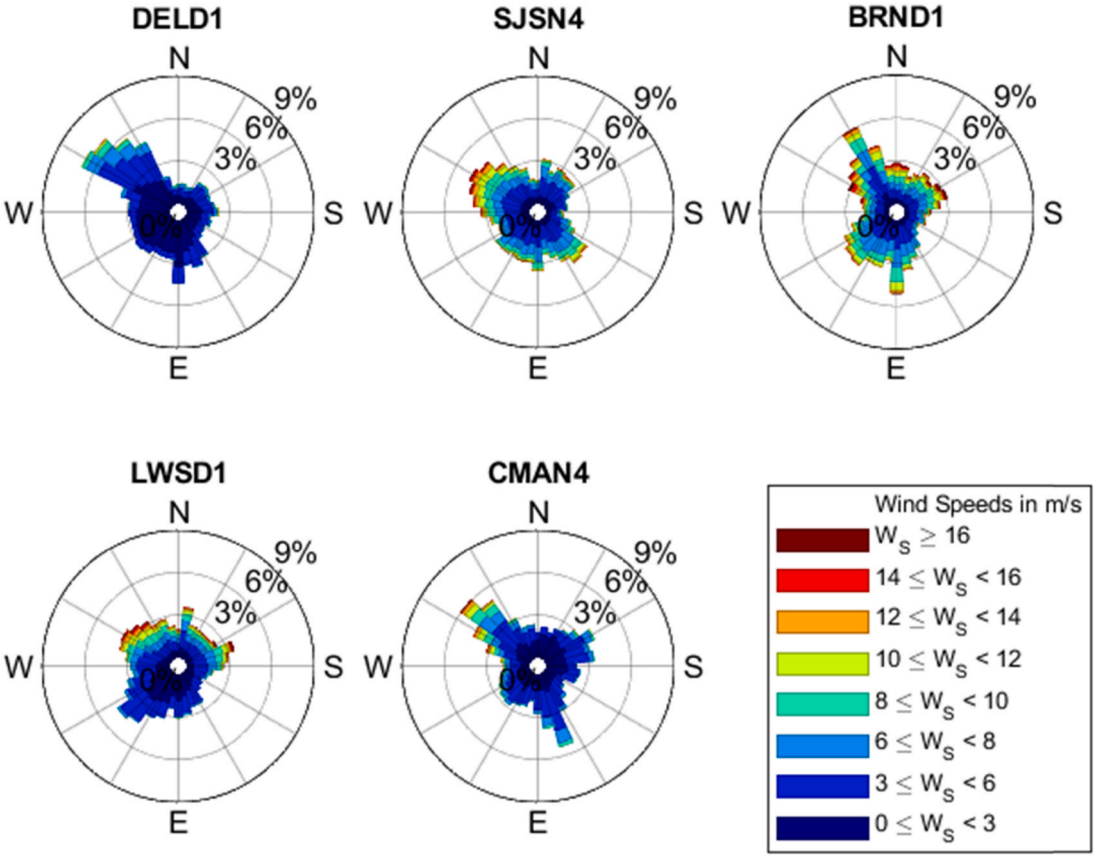

Fig. 3. Wind roses measured at stations DELD1, SJSN4, BRND1, LWSD1, and CMAN4 in 2015 and 2016.

variations of wind fields in Delaware Bay (Fig. 3). This finding is consistent with the statement in Kukulka et al. (2017), indicating that the relationship between the wind forcing and wave responses may not be thoroughly explored if the wind data from only one or two stations are applied. Additionally, the measured H_s at WG3 exhibited a high dependency on the wind speed at all five stations (Fig. B1 (a)). Therefore, we employed the wind data at all five stations from January 2015 to October 2020 for further analysis in this study. However, there are blocks of missing data (about 9%) at the five stations during the study period (Table 1). To facilitate the wave climate prediction in 2015, 2016, 2018, 2019, and 2020, the missing wind data over the five years were filled first before quantifying the changes of wave power across the CORs over the years (Section 2.3.3).

2.3.2. *Representativeness of the wind field and water level over the 2-month deployment*

In this study, a representative test was utilized to examine whether the measured wave parameters during the two months can be used to predict long-term wave processes. This step is necessary because ANN models cannot generalize to estimate scenarios that are unseen in the training dataset (Willard et al., 2020). Given that the wind speed, wind fetch, and water depth are critical to predicting wind waves in a shallow estuary (Karimpour et al., 2017), we investigated whether the wind and water depth combinations during the two months of 2018 can represent the ones throughout the years (i.e., in 2015, 2016, 2018, 2019, and 2020). The water level measurement at station SJSN4 (Fig. 1 (a)) was used to represent the water depth at the study site since it is closest to the CORs. Hereafter, the wind and water depth combination is considered as the forcing of wind wave generation in this work.

The following steps were taken to quantify the representativeness of the forcing of wave generation during the two months. First, the hourly datasets of wind direction, wind speed, and water level during the two months of 2018 and in 2015, 2016, 2018, 2019, and 2020 were uniformly divided into 36 directional bins (i.e., 0°-10°, 10°-20°, 20°-30°, …, 350°-360°), 60 speed bins (i.e., 0–0.5, 0.5–1, 1–1.5, …, 29.5–30 m/s), and 20 water level bins (i.e., −2∼-0.18, −0.18∼-0.16. −0.16∼-0.14, …, 1.8–2 m), respectively. The three groups of bins were then combined into 43,200 cubic divisions (i.e., $36 \times 60 \times 20 = 43{,}200$). A forcing was considered representable by the 2-month forcings if that specific data fell into one of the divisions that were also taken by the 2-month data. Fig. 4 shows an example of hourly wind direction, wind speed, and water level data at DELD1 in 2019 versus the ones in February and March 2018. To better visualize the dataset, we projected the three-dimensional space into two-dimensional spaces (i.e., Fig. 4 (b), Fig. 4 (c), and Fig. 4 (d)) with meshes representing the bins of wind speed, wind direction, and water level.

Note that the wind fetch plays a significant role in generating wind waves in shallow estuaries (Karimpour et al., 2017). The wave height at the study site could be exceedingly small when winds were from specific directions because of a short fetch. Table 2 presents the wind directions at different stations corresponding to small wave height measured at WG3 from January 31 to April 2, 2018 (Fig. B1 (b)). In other words, the fetch would be so short that winds have very limited influence on the wave field at the study site if the wind direction is within the listed range

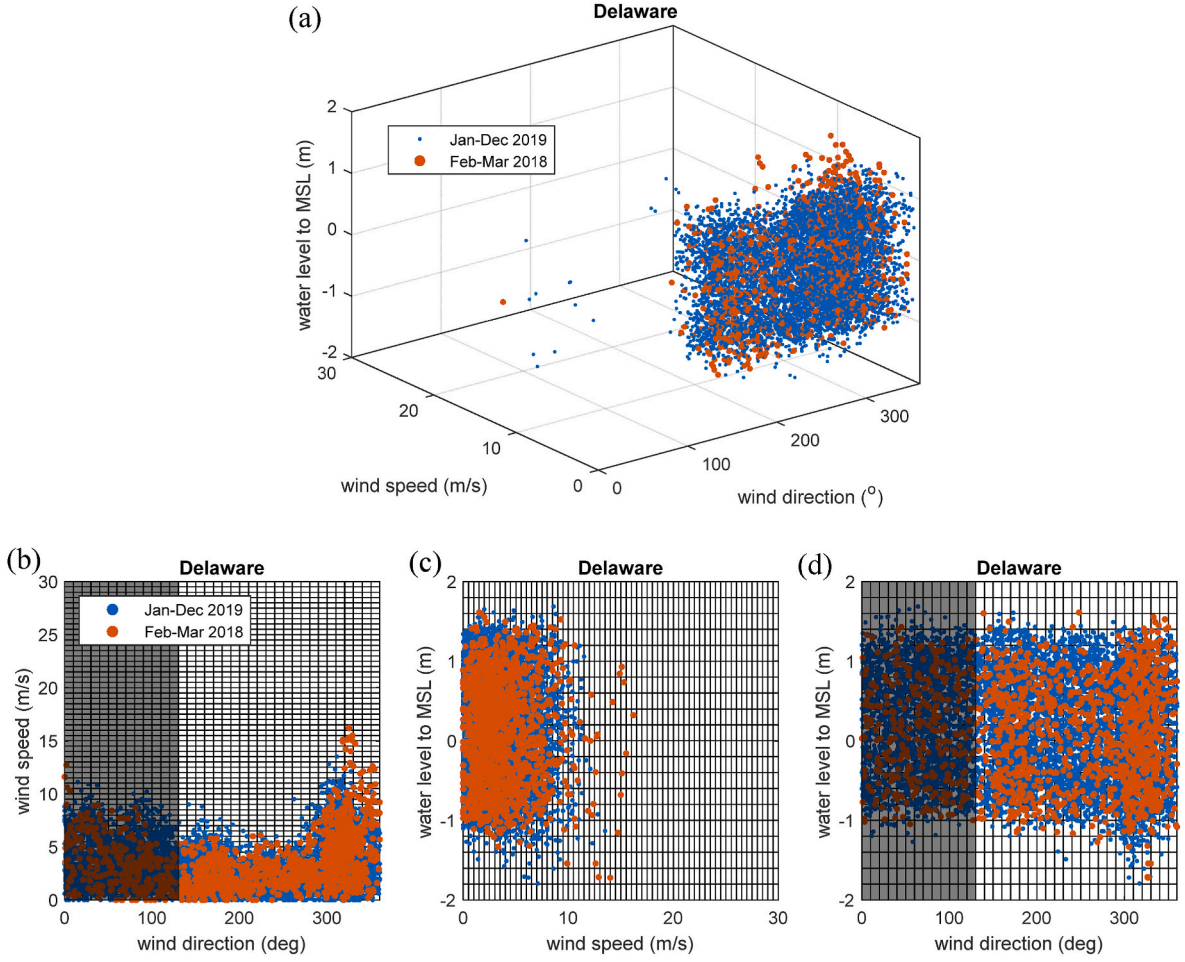

Fig. 4. (a) Hourly wind direction, wind speed, and water level data at DELD1 in 2019 versus February and March 2018. (b) wind direction and wind speed at DELD1 in 2019 versus February and March 2018. (c) wind speed and water level at DELD1 in 2019 versus February and March 2018. (d) wind direction and water level at DELD1 in 2019 versus February and March 2018. The black blocks correspond to the wind direction listed in Table 2.

Table 2
The wind directions at different stations that have little influence on the wave field at the study site.

Stations	DELD1	SJSN4	BRND1	LWSD1	CMAN4
Wind direction	0°- 130°	0° - 130°	0° - 150°	0° - 140°	0° - 100°

Table 3
The percentages of forcings of wave generation in different years that can be represented by the 2-month data in 2018.

	DELD1	SJSN4	BRND1	LWSD1	CMAN4
2015	96.1%	94.5%	95.8%	95.3%	94.2%
2016	95.1%	92.1%	95.1%	94.8%	93.0%
2018	95.0%	91.1%	94.5%	93.9%	92.4%
2019	95.2%	95.3%	95.0%	93.3%	92.2%
2020	95.1%	94.5%	94.1%	93.6%	92.7%

in Table 2. Since waves with small energy (e.g., smaller than 0.2 m at WG3) are less critical to examining the influence of CORs in this study, wind data at different stations were exempt from the representative test if the wind direction is within the range listed in Table 2. However, it is worth emphasizing that the composite wave models were developed using all available wind data (0°-360°) to ensure the obtained models could be predictive in general scenarios.

The results indicate that the average percentage of annual forcings that could be represented by the 2-month data was 94.2% at the five stations in 2015, 2016, 2018, 2019, and 2020 (Table 3). Given that the 2-month forcings of wave generation could largely represent the ones over the five years, the short-term measured wave parameters could be applied to develop ANN models to predict wave parameters at the study site over the five years.

2.3.3. Wind data prediction

To estimate the wave climate in 2015, 2016, 2018, 2019, and 2020, the missing wind data over the five years were filled first because it significantly affected the wave field at the study site. Thus, two ANN wind models were developed to fill gaps in the wind dataset at SJSN4 and BRND1 in 2018, 2019, and 2020 based on the data in 2015 and 2016, when the wind data were available almost all the time. Specifically, ANN wind models were first trained, validated, and tested with the dataset in 2015 and 2016. Then the missing data at the two stations in 2018, 2019, and 2020 were filled with the predictions from the developed ANN wind models. Table 4 shows the input features and labels of ANN models for simulating wind data at SJSN4 and BRND1. The input features were selected based on the locations and availability of the wind data at different stations. For example, winds at LWSD1 and CMAN4 were used to fill the gaps at BRND1, considering both locations (Fig. 1 (a)) and the data availability (Table 1) at these two stations.

The network structure of three hidden layers of 30 nodes was applied for estimating the missing wind data at SJSN4 and BRND1 stations. The testing and validation data for both ANN models contained continuous hourly datasets from January 01, 2016 to 03/15/2016 and January 04, 2016 to 06/15/2016, respectively. The training data included the rest of the dataset in 2015 and 2016. Hyperbolic Tangent was applied as the activation function. Levenberg-Marquardt backpropagation (μ = 0.001) was used as the network training function. Normalization was applied to keep the input and output between −1 and 1 so that the negative influence of the large difference between different parameters could be avoided. The Nguyen-Widrow method was employed for initializing the weight and bias values for each layer. Early stopping was applied to simulations to prevent overfitting. Specifically, the training was terminated when the validation error increased for six iterations, and weights and biases were returned at the minimum of the validation error. The MATLAB Deep Learning Toolbox was utilized to develop the ANN wind models.

Table 4
The input features and labels of ANN models for predicting wind data at BRND1 and SJSN4.

Wind models	Input features	Labels
BRND1	*u*- and *v*-wind speed data at LWSD1 & CMAN4	*u*- and *v*-wind speed data at BRND1
SJSN4	*u*- and *v*-wind speed data at DELD1 & BRND1	*u*- and *v*-wind speed data at SJSN4

2.3.4. Water depth and wave data prediction

In this study, four composite wave models were trained and validated to estimate d (local water depth), H_s, and T_p based on the measured wave characteristics at WG3, WG6, WG5, and WG1 from January 31 to April 2, 2018. Then the developed composite wave models were applied to simulate wave parameters at the study site in 2015, 2016, 2018, 2019, and 2020. The composite networks combining long short-term memory (LSTM) and ANN were designed based on prior knowledge of wave responses to forcing functions and the relationship between wave parameters. Specifically, the hourly *u*- and *v*-wind speed and water level data measured at the NOAA stations were applied as inputs for simulating local water depth (d) at each wave gauge location using the LSTM method (Table 5, Fig. 5). Then the network for modeling H_s was developed with wind and water depth data as input features. Given that the information of H_s is also essential for predicting T_p, H_s was further used as the input together with the wind and water depth for the T_p prediction (Table 5). As a result, the loss function of the entire composite network was defined as the sum of error functions of d, H_s and T_p. It is worthwhile to mention that although three independent networks could also be utilized for predicting d, H_s, and T_p separately, they were not applied in this study as the error propagation could occur when the predicted d and H_s were taken as inputs for estimating T_p by another independent ANN model. The composite networks proposed in this study can reduce error propagation by estimating d, H_s, and T_p simultaneously with a unified network architecture, as shown in Fig. 5.

Pytorch was employed for developing the composite networks in this study. The maximum learning epoch and mean square error (*MSE*, defined in Appendix A) of predicted parameters were used to control the training procedure. Specifically, the training procedure was stopped once the iteration number reached 1000 or one of the *MSE*s of d, H_s, or T_p ceased to decrease. The sequence length for the LSTM models was set to 24. Hyperbolic Tangent was applied as the activation function. The initial weights in each layer were set to follow Xavier normal distribution (Glorot and Bengio, 2010), and the initial biases were all set to zero. Normalization was employed to keep inputs and outputs between −1 and 1 so that the negative influence of the significant difference between various parameters could be avoided. The Adam (adaptive moment estimation) optimization algorithm was used as the network training function (Kingma and Ba, 2014). The initial learning rate was set to 0.01 and then decreased to 0.001 after 500 iterations. The training was performed on an Intel Core i7 with 32 GB memory, and the cost was approximately 30 s.

The network structure can have a crucial influence on the prediction skill of ANNs. Therefore, 1,164 ANNs (2–5 hidden layers of 10–300

Table 5
Input features and labels for predicting d H_s, and T_p using composite networks.

Prediction	Input features	Labels
d	*u*- and *v*-wind speed data at SJSN4 & BRND1, water level data from SJSN4	Measured d at each gauge location
H_s	*u*- and *v*-wind speed data at all five stations, predicted d at each gauge location	Measured H_s at each gauge location
T_p	*u*- and *v*-wind speed data at all five stations, predicted d, and H_s at each gauge location	Measured T_p at each gauge location

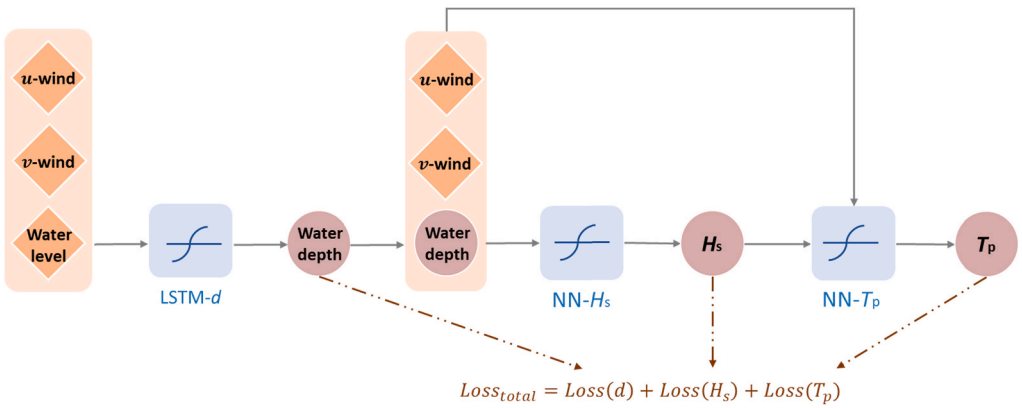

Fig. 5. Schematic architecture of the composite neural networks for predicting d, H_s, and T_p at each gauge location in 2015, 2016, 2018, 2019, and 2020.

Fig. 6. The dataset separation for the 5-fold block cross-validation.

nodes) were created to determine the optimum network structure for each composite wave model at different gauge locations. The number of hidden layers and nodes for networks to simulate d, H_s and T_p was kept the same. To quantify the prediction skills of composite networks with different structures, the composite performance score (*CPS*) was calculated based on error matrices, including *bias*, *SI*, and R^2 (Appendix A). As a result, the structure providing the highest total composite performance score (*TCPS*), which equals the mean value of *CPS*s for the prediction of d, H_s, and T_p, was considered to be the optimal one.

Given the limited data samples in this study, a 5-fold block cross-validation method was used for selecting the optimum network structure for each ANN wave model (Fig. 6). The testing dataset contained continuous hourly data from March 10 to March 15, 2018 (dark orange part in Fig. 6), which was employed as an independent measurement of network ability after training. During this period, large waves were observed at the study site due to nor'easter Skylar, so the prediction skills of the developed composite models could be well tested. The rest of the dataset was then partitioned into five blocked subsamples. For each structure, the network was trained five times separately so that every subsample was utilized once for validation (Zheng et al., 2020). As a result, five *TCPS*s could be obtained based on the validation results for each structure, and the mean value was used to represent the prediction performance of the particular structure. The optimal network structure was identified by comparing the *TCPS*s of all structures.

3. Results

3.1. Filling the missing wind data using ANN wind models

As part of the wind data were missing at stations SJSN4 and BRND1 during the study period (Table 1), ANN wind models were trained to fill the gaps so that wave conditions around CORs could be examined throughout the years. Fig. 7 shows the comparison between observed and predicted easterly and northerly wind components at SJSN4 in 2015 and 2016. The results show that the prediction ability of the ANN wind model at station SJSN4 is high, with the R^2 value around 0.87 and *RMSE* around 1.65 m/s.

To further validate the ANN wind model at SJSN4, the simulated wind data were compared with available measurements at SJSN4 in 2018 (Fig. B2). The small *RMSE* values of predicted wind components indicated that the developed ANN wind model could fill missing wind data at SJSN4 with sufficient accuracy. The same procedure was carried out to fill data gaps at BRND1 with the data at LWSD1 and CMAN4 as inputs (Table 4). The results show that the developed wind ANN model at BRND1 also has an excellent prediction ability. Therefore, all missing wind data at SJSN4 and BRND1 were filled by the ANN wind models, so that the wave power variation across the CORs can be examined throughout the years.

3.2. Wave field simulation by composite networks

To determine the optimal network structures for composite wave models, a total of 1,164 structures (2–5 hidden layers with 10–300 nodes per layer) were examined with the 5-fold block cross-validation method for simulating wave parameters at each WG location. Fig. 8 shows an example of *TCPS*s generated by selected composite wave models with different network structures at WG3 (2–5 hidden layers with 8, 16, 32, 64, 128, 256 nodes per layer). The results indicate that the simulation skills are similar when the networks have 2 or 3 hidden layers. The model shows overfitting patterns when the structure has 3 or 4 layers with more than 200 nodes per layer, reducing the simulation accuracy. The optimal structure for the network at WG3 was identified as 3 hidden layers of 12 nodes with the highest *TCPS* of 0.92. The optimal ANN structures for modeling wave parameters at other WG locations are shown in Table D1.

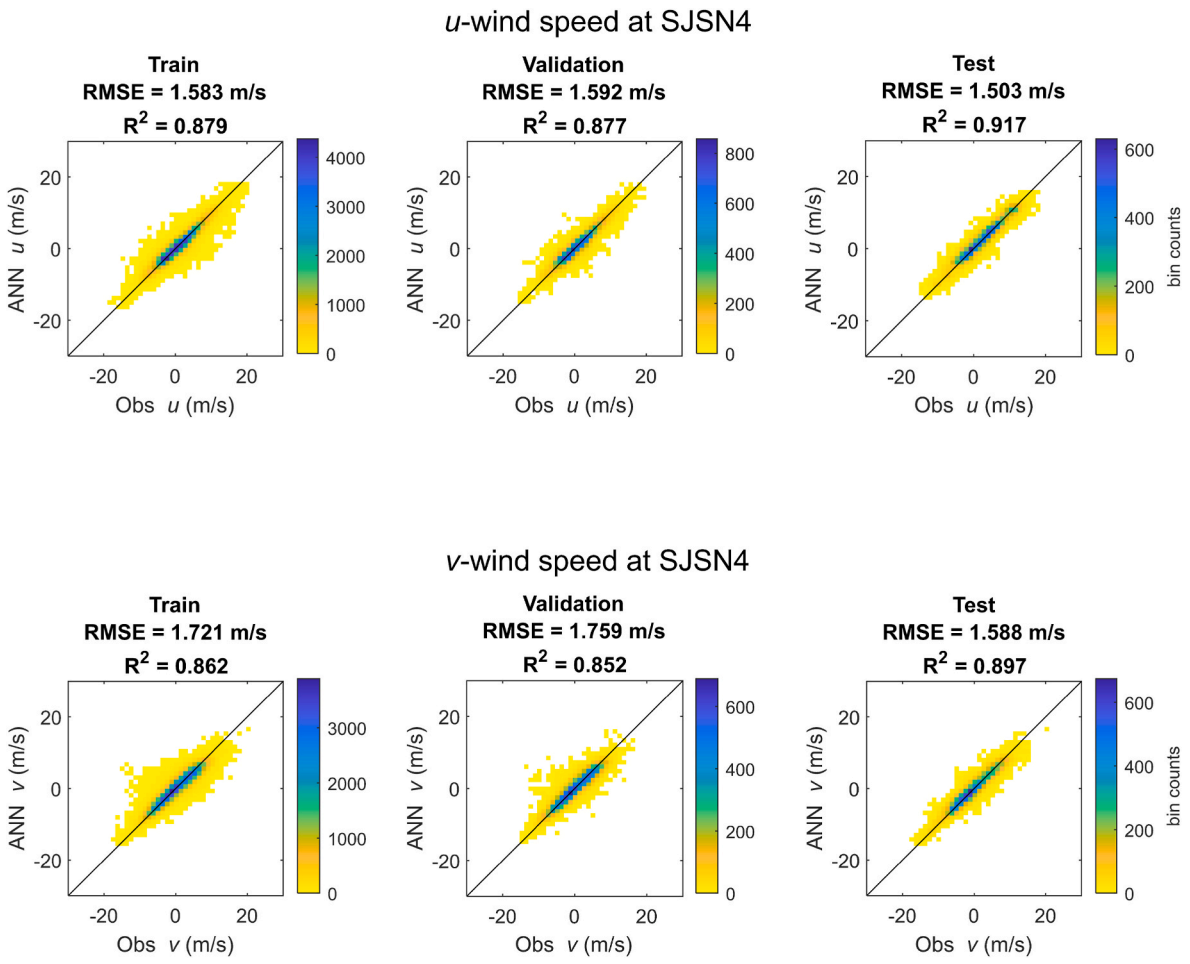

Fig. 7. Comparison between the observed and ANN-predicted easterly and northerly wind components at SJSN4 in 2015 and 2016. The positive values of u- and v-wind represent the westerly and southerly wind components, respectively. The negative values of u- and v-wind correspond to the easterly and northerly wind components, respectively. Different colors correspond to different counts of data points in each bin (50 bins were specified in x and y directions). (For interpretation of the references to color in this figure legend, the reader is referred to the Web version of this article.)

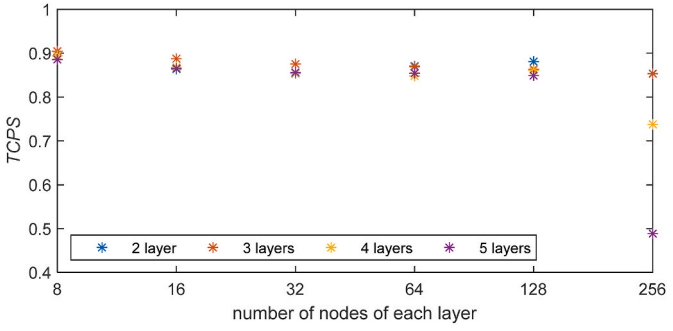

Fig. 8. The TCPSs generated by the composite wave models at WG3 with different network structures.

3.2.1. Prediction of local water depth

Fig. 9 shows the modeled local water depth versus observations at each gauge location during the testing phase from March 10 to March 15, 2018. The results revealed that the prediction skills of all four models were very high, with R^2 and RMSE values close to 0.96 and 0.094 m, respectively. The developed composite models were then applied to estimate local water depth in 2015, 2016, 2018, 2019, and 2020 so that the wave field around the CORs could be examined over the years.

3.2.2. Prediction of H_s and T_p

The comparisons between the simulated and measured H_s and T_p during the testing phase are shown in Fig. 10 and Fig. 11. The composite wave models showed high prediction skills for simulating H_s at each WG location, with R^2 values around 0.85 and *RMSE* around 0.06 m. The simulation accuracy of T_p was slightly lower, with R^2 values around 0.70 and *RMSE* around 0.35 s. Therefore, the four composite models can be expected to hindcast wave parameters of H_s and T_p with sufficient accuracy during the years of 2015, 2016, 2018, 2019, and 2020. The time series of the predicted and observed wave parameters at WG3 and WG5 in 2018 are presented in Fig. C1.

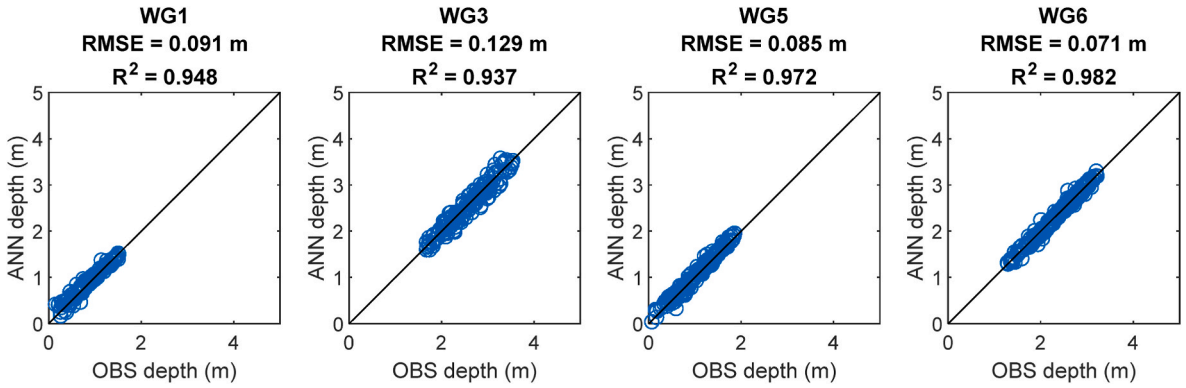

Fig. 9. Comparison between the measured and simulated local water depth at each gauge location (only contain the testing data).

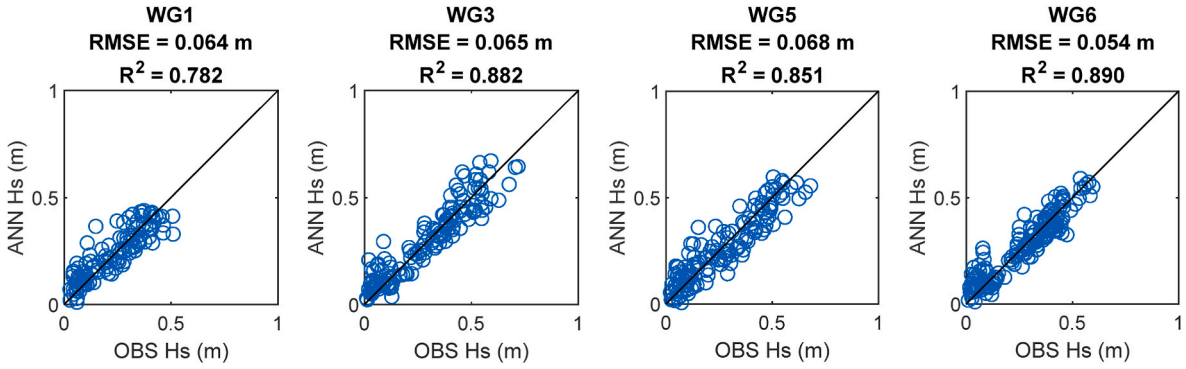

Fig. 10. Comparisons between measured and predicted H_s at different gauge locations in 2018 (only contain the testing data).

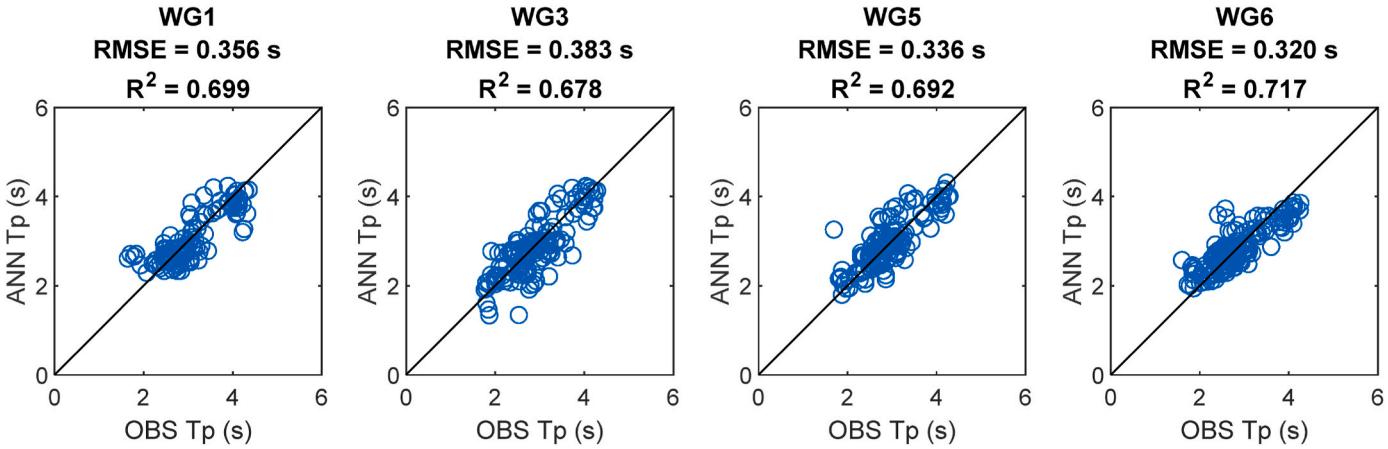

Fig. 11. Comparisons between measured and predicted T_p at different gauge locations in 2018 (only contain the testing data).

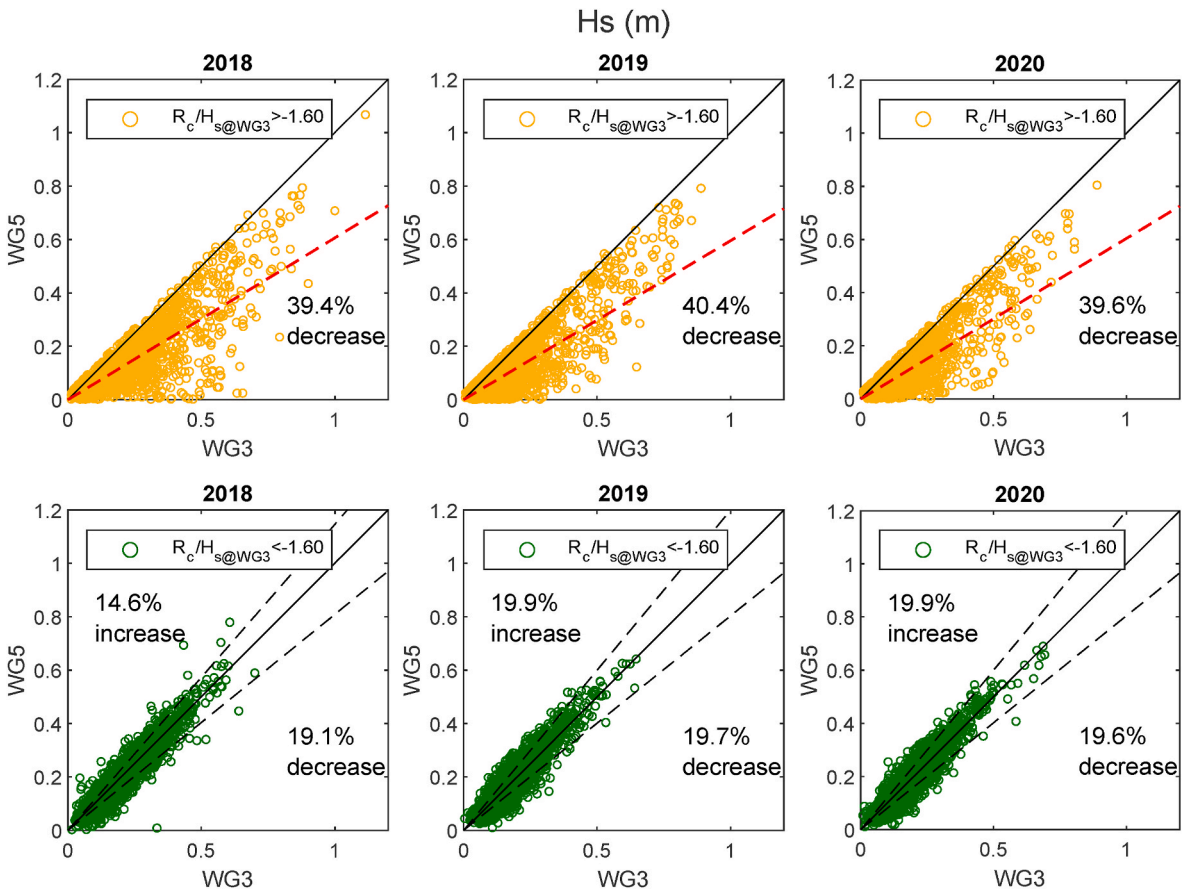

Fig. 12. Comparisons between H_s at WG3 and WG5 during the years 2018, 2019, and 2020.

4. Discussion

4.1. Spatial variations of wave heights

To examine the wave height variation across the living structures in Gandys Beach, H_s offshore to CORs (WG3) and H_s protected by CORs (WG5) were compared during the years 2018, 2019, and 2020 (after the construction of oyster reefs). According to Zhu et al. (2020), a significant correlation can be observed between the wave height variations and the ratio of the crest freeboard (R_c) to offshore wave heights. Therefore, we used $R_c/H_{s,\,WG3}$ as an indicator for investigating the wave height changes across the CORs, as it could combine wave properties and structure characteristics (Wiberg et al., 2019). In this study, R_c was defined as the vertical distance from the water surface to the crest of CORs. The reef crest was considered as emergent, slightly submerged, and fully submerged when $R_c/H_{s,\,WG3} > 0$, $-1.6 < R_c/H_{s,\,WG3} < 0$, and

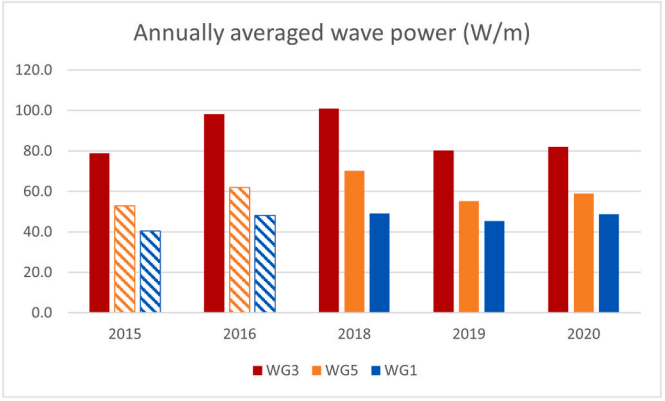

Fig. 13. The annually averaged wave power at WG3, WG5, and WG1 in 2015, 2016, 2018, 2019, and 2020. The CORs have not been constructed until the summer of 2016, so the wave powers at WG1 and WG5 were not real in 2015 and 2016 and marked with dashed lines in the plot.

Table 6
The annually averaged wave power at WG3, WG5, and WG1 in 2015, 2016, 2018, 2019, and 2020. The CORs have not been constructed until the summer of 2016, so the wave powers at WG1 and WG5 were not real in 2015 and 2016.

	Wave power (W/m)			Wave power reduction from WG3 to WG5
	WG3	WG5	WG1	
2015	78.9	52.8	40.5	33.1%
2016	98.1	61.9	48.1	36.9%
2018	101.0	70.3	49.2	30.4%
2019	80.4	55.2	45.3	31.3%
2020	82.0	58.9	48.8	28.1%

Table 7
The top 50% wind speed at each station and the percentages of wind data met both requirements over the five years.

	DELD1	SJSN4	BRND1	LWSD1	CMAN4
Top 50% wind speed	2.7 m/s	5.5 m/s	6.7 m/s	4.2 m/s	3.6 m/s

	DELD1	SJSN4	BRND1	LWSD1	CMAN4	Average
2015	28.2%	33.6%	28.2%	25.0%	30.4%	29.1%
2016	30.4%	40.5%	31.8%	28.9%	34.6%	33.3%
2018	31.8%	34.4%	37.3%	29.8%	36.7%	34.0%
2019	28.8%	24.5%	24.3%	24.9%	30.3%	26.6%
2020	28.8%	26.9%	28.0%	25.1%	27.0%	27.1%

$R_c/H_{s,\ WG3} < -1.6$, respectively.

Fig. 12 compares the predicted H_s at WG3 and WG5 in 2018, 2019, and 2020. The results show that during low tides ($R_c > -1.6H_{s,\ WG3}$), an average reduction rate of 39.8% in wave height (reduction rate $= (H_{s,\ WG3} - H_{s,\ WG5})/H_{s,\ WG3}$) can be observed from the most offshore station (WG3) to the nearshore station behind CORs (WG5) over the three years. Note that complex nearshore wave transformation occurred between WG3 and WG5. The observed wave height changes from WG3 to WG5 were mainly caused by the combined effect of bathymetric changes (e.g., depth-limited wave breaking at low tides) and the CORs (Zhu et al., 2020). Also, the Nantuxen point to the northwest of the study site could provide a shelter effect and reduce the wave height at WG5. While, during high tides, the wave height from WG3 to WG5 had an average rate of 19.7% reduction to 19.9% amplification over the three years. This can be explained by the fact that the wave shoaling and wave breaking could happen simultaneously when the reef crest was fully submerged. To validate this finding, we calculated the shoaling coefficient ($K_{s,\ WG5}$) and the ratio between wave height and local water depth (wave breaks when $H_{s,\ WG5}/d_{WG5} > 0.6$) based on Battjes and Janssen (1978). The results indicate that shoaling and breaking happen simultaneously during the high tide conditions with $R_c < -1.6H_{s,\ WG3}$. Moreover, it was found that wave focusing occurred in the leeside area behind CORs during high tide conditions due to combined wave refraction and diffraction (Zhu et al., 2020). As a result, wave energy could easily transmit to the leeside area behind the structures with high water levels.

The above findings of the effectiveness of CORs on wave height attenuation in 2018 are consistent with the analysis of Zhu et al. (2020), which focused on exploring the wave climate and wave spectral variation at the same study site using measured data from January 31 to April 2, 2018. They found that an average reduction rate of 41% in wave height was observed from WG3 to WG5 at low tide conditions during the two months. Also, they demonstrated that the wave height variation between WG3 and WG5 ranged from a 35% reduction to a 70% increase during high tide conditions, in line with our results. It is worth emphasizing that bathymetric refraction and depth-limited wave breaking play an important role in the observed wave height reduction and amplification across the CORs.

4.2. Wave power changes across the CORs

Wave parameters and local water depth data simulated by the data-driven models were utilized to calculate wave power P with the following equation:

$$P = \frac{\rho g H_s^2}{16} c_g \tag{1}$$

where c_g is wave group velocity and ρ is water density. Fig. 13 and Table 6 summarize the annually averaged wind sea wave power at WG3, WG5, and WG1 in 2015, 2016, 2018, 2019, and 2020. Since CORs have not been constructed until the summer of 2016, wave powers at WG1 and WG5 in 2015 and 2016 were not real and were marked with dashed lines in the plots to avoid confusion. The results show that the annually averaged wave power reduction rate from WG3 to WG5 was about 30.0% in 2018, 2019, and 2020 (Table 6). Therefore, the wave power offshore could be effectively reduced across the living shoreline project area at the study site owing to both the nearshore bathymetric effect and the CORs.

The results show that the annually averaged wave power generally increased from 2015 to 2018, then went down in 2019 and went up again in 2020 at the study site. To validate this pattern, the wind conditions were further investigated over the five years since wind is the driving force of wind seas. The percentage of winds with high speed and long fetch distance was computed at each station over the five years (Table 7). Specifically, the percentage of winds that satisfied both of the following requirements were calculated: (a) the wind direction was outside the range listed in Table 2, and (b) the wind speed was the top 50% of data at each station over the five years. As a result, the percentages of winds (averaged over stations) that met both conditions are 29.1% in 2015, 33.3% in 2016, 34.0% in 2018, 26.6% in 2018, and 27.1% in 2020, consistent with the observed variation pattern of the annually averaged wave power shown in Fig. 13.

This study did not include swell wave variation analysis since swell energy remains nearly unchanged on the seaward and shoreward sides of CORs (Zhu et al., 2020; Wang et al., 2021). However, it is worth mentioning that the proposed framework can also be used to estimate swell waves with different input features and labels. Specifically, the input features include wave boundary conditions (i.e., outside the bay) and water levels, and the labels are the swell wave parameters (e.g., H_s and T_p). Furthermore, the test of data representativeness is also required before using the developed model for predicting swell waves over multiple years. In other words, we need to validate if the input features for predicting swell waves over the years can be represented by the ones during short-term field measurements.

5. Conclusions

Recently, many living shoreline projects have been built to restore and protect coastal ecosystems along the U.S coasts. A deeper understanding of the wave power variation around the living shoreline structures at different time scales can help to achieve long-term ecological benefits. In this study, we investigated the long-term wave characteristics across the CORs based on the short-term wave measurements in Gandys Beach in upper Delaware Bay. Six wave gauges were deployed in Gandys Beach from January 31 to April 2, 2018, providing an informative dataset of the wave climate around the CORs during winter storms. This study developed a framework to estimate long-term wind wave characteristics based on the short-term representative wave measurements using soft computing-based models (i.e., ANN and LSTM), which enabled the examination of the wave power variation across the CORs over multiple years.

The wind field in Delaware Bay was investigated first since it is the main driving force of wind seas. Due to the significant variability in estuarine wind fields, the wind data from five NOAA stations at DELD1, SJSN4, BRND1, LWSD1, and CMAN4 were employed in the analysis. ANN wind models were developed to fill the missing data at SJSN4 and BRND1 during the study period. Then the representativeness of the wind and water level during the two months in 2018 was tested to determine whether the measured wave parameters could be employed for studying the wave field over multiple years. It was found that the average percentage of annual forcings that could be represented by the 2-month data was 94.2% in 2015, 2016, 2018, 2019, and 2020. Given that the 2-month forcings of wave generation could largely represent the ones over the five years, the short-term measured wave parameters were used to train ANN models for studying the wave height changes across the nearshore with the CORs throughout the years. Thus, based on the 2-month wave measurements, four composite ANN networks were developed to estimate wave parameters at WG3, WG6, WG5, and WG1 using the wind and water levels as input features. The composite ANN models showed high prediction skills for simulating d, H_s, and T_p at each

sensor location, with the values of R^2 around 0.96, 0.85, and 0.70, respectively. Therefore, the developed models could hindcast the wave parameters in 2015, 2016, 2018, 2019, and 2020 with sufficient accuracy.

To examine the wave height variations across the living shoreline project area, we compared H_s offshore to the CORs and H_s protected by the CORs at the study site. The results show that the wave energy could be considerably reduced when the oyster reef crests were emergent or slightly submerged, leading to wave height reduction by an average rate of 39.8% in 2018, 2019, and 2020. The wave height attenuation at the study site was mainly caused by the combined effect of bathymetric changes and the CORs. Also, the landmass at the Nantuxen point to the northwest of the study site could provide a sheltering effect and reduce the wave height at WG5. During high tide conditions, wave shoaling and breaking could occur simultaneously, and a significant amount of wave energy could transmit to the leeside of the structure. Moreover, it was found that the annually averaged wave power reduction from WG3 to WG5 was about 30.0% in 2018, 2019, and 2020 owing to both the bathymetric effect and CORs.

In closing, our analysis in this study provides a framework for forecasting long-term wave characteristics based on long-term wind and short-term wave measurements. Although this approach only provides the location-specific wave prediction, it can be used as a tool to obtain a fast estimation of the long-term wave climates when location-specific wave predictions are needed. Furthermore, this approach has an advantage over the traditional numerical models as it requires much lower computational costs. To predict wave fields with this framework robustly, the available wave measurements are required to be representative of the wave climate over the years, so that ANNs can better learn the nonlinear relation between input features and outputs. Thus, it is essential to ensure that the deployment period is long enough to record the wave climate when extreme or representative events happen. Overall, the data and information about the annual wave power estimates in this study are helpful for understanding and predicting wave-induced marsh edge erosion and shoreline retreat. The proposed framework of developing composite neural networks to estimate long-term wave characteristics based on short-term wave measurements can be applied to other estuaries and coasts.

CRediT authorship contribution statement

Nan Wang: Methodology, Software, Writing – original draft, preparation. **Qin Chen:** Conceptualization, Methodology, Investigation, Writing – review & editing, Supervision, Funding acquisition. **Ling Zhu:** Investigation, Data curation, Writing – review & editing. **Hongqing Wang:** Investigation, Resources, Writing – review & editing.

Declaration of competing interest

The authors declare that they have no known competing financial interests or personal relationships that could have appeared to influence the work reported in this paper.

Acknowledgments

Funding for the study has been provided in part by the National Fish and Wildlife Foundation (NFWF, Project #55032) and the National Science Foundation (NSF Grants 1856359 and 2139882). We thank Dr. Zhangping Wei and two anonymous reviewers for their constructive reviews on the improvement of the manuscript. Any use of trade, firm, or product names is for descriptive purposes only and does not imply endorsement by the U.S. Government. Data associated with this paper are available in Wang et al. (2020).

Appendix A. Error metrics

Statistical measures given below are utilized to evaluate the performance of the developed models.

MSE:	$MSE = \frac{\sum_i^N (y_i - \hat{y}_i)^2}{N}$	(A.1)
RMSE:	$RMSE = \sqrt{\frac{\sum_i^N (y_i - \hat{y}_i)^2}{N}}$	(A.2)
SI:	$SI = \frac{RMSE}{\bar{y}}$	(A.3)
bias:	$bias = \frac{1}{N}\sum_i^N \hat{y}_i - y_i$	(A.4)
R^2:	$R^2 = \left(\frac{\sum_i^N (y_i - \hat{y}_i)^2}{\sqrt{\sum_i^N (y_i - \bar{y}_i)^2 \sum_i^N (\hat{y}_i - \bar{\hat{y}}_i)^2}}\right)^2$	(A.5)
Normalized *SI* performance:	$\widetilde{SI} = 1 - SI$	(A.6)
Normalized *bias* performance:	$\widetilde{bias} = 1 - \frac{abs(bias)}{\bar{y}}$	(A.7)
Composite Performance Score:	$CPS = \frac{R^2 + \widetilde{SI} + \widetilde{bias}}{3}$	(A.8)
Total composite performance score:	$TCPS = \frac{1}{3}(CPS_d + CPS_{H_s} + CPS_{T_p})$	(A.9)

in which N is the number of samples, $\hat{y}_i$ is the estimated values, and y_i is the true value.

Appendix B. Wind data

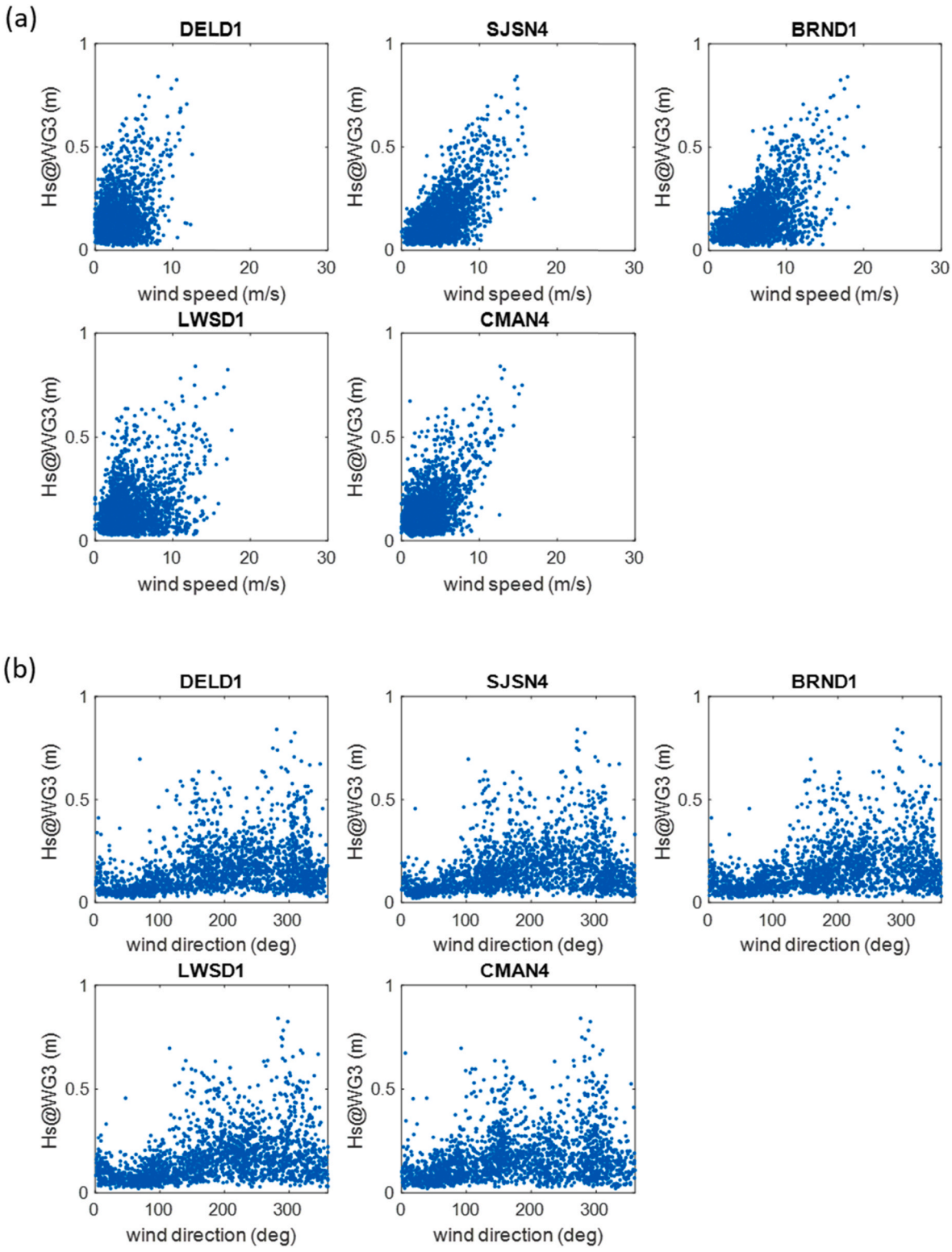

Fig. B.1. The measured Hs at WG3 versus the measured (a) wind speed and (b) directions at the five stations from January 31 to April 2, 2018.

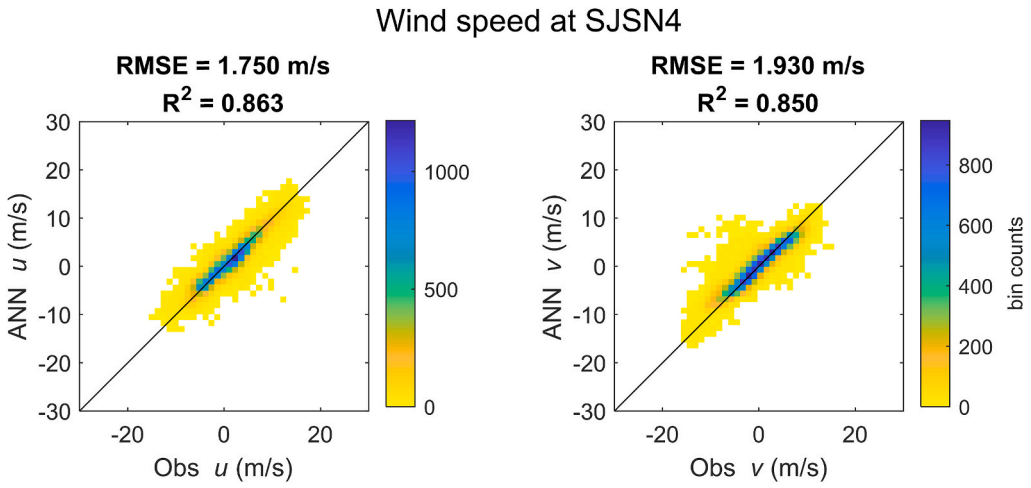

Fig. B.2. Comparison between the observed and ANN-predicted easterly and northerly wind components at SJSN4 in 2018.

Appendix C. Wave parameters

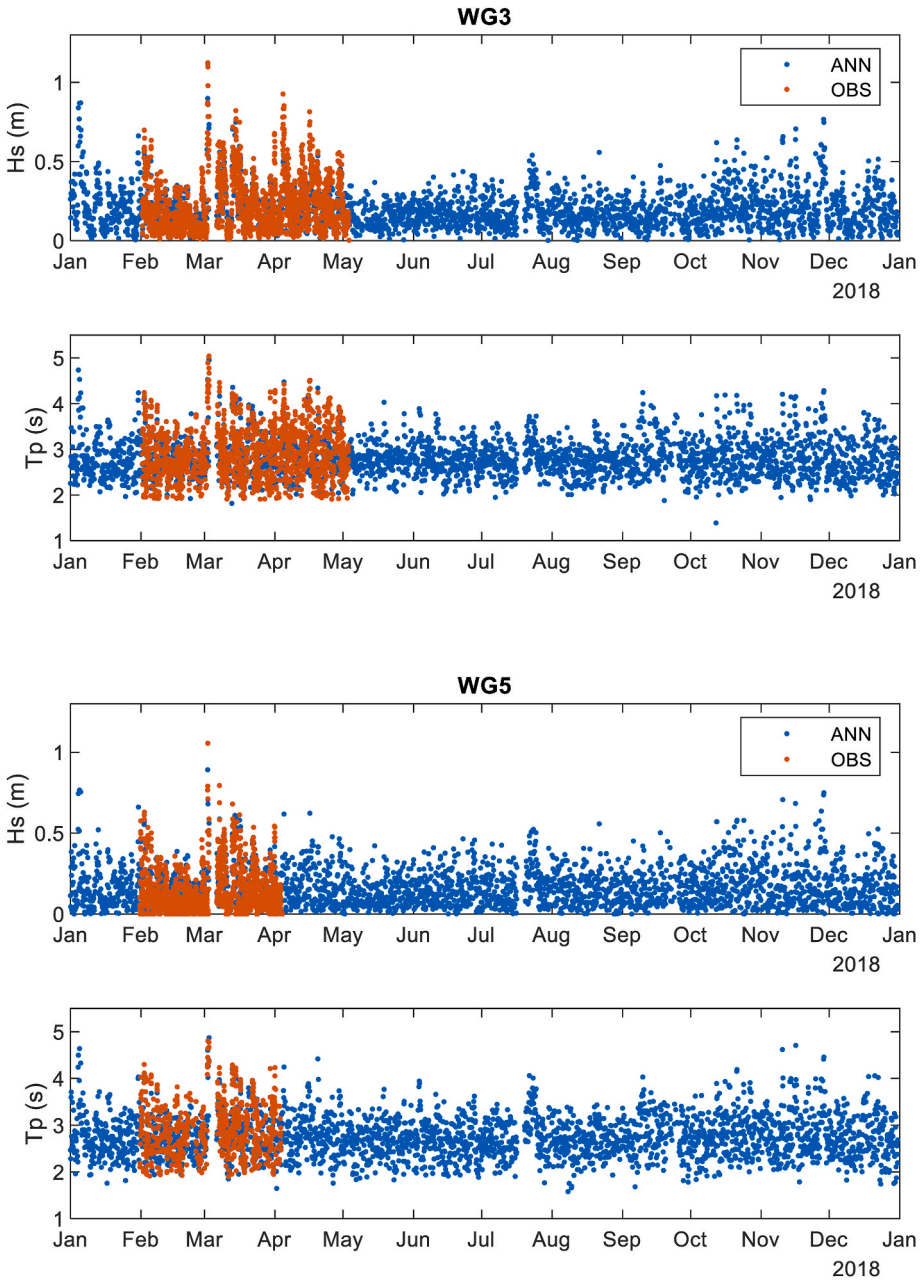

Fig. C.1. The time series of measured and predicted H_s and T_p at WG3 and WG5 in 2018.

Appendix D. ANN wave model structures

Table D.1
Optimal structures of ANN models for predicting wave parameters at different wave gauge locations.

	WG1	WG3	WG5	WG6
Number of hidden layers	3	3	2	2
Number of nodes in each layer	21	12	40	26

Appendix E. Photos of living shoreline structures

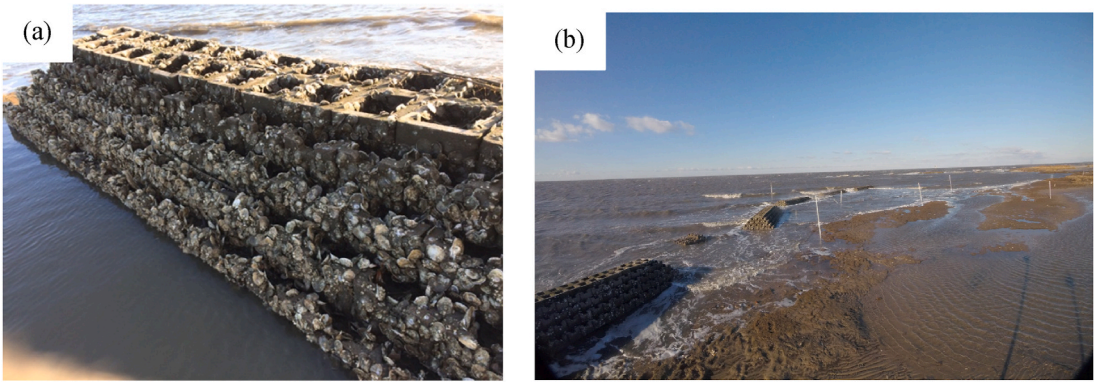

Fig. E.1. Photographs of the constructed oyster reefs taken at the study site at 9:00 a.m. on February 5, 2018 (Photo credits: (a) Qin Chen and (b) Hongqing Wang).

References

Baker, A.J., Gonzalez, P.M., Piersma, T., Niles, L.J., de Lima Serrano do Nascimento, I., Atkinson, P.W., Clark, N.A., Minton, C.D.T., Peck, M.K., Aarts, G., 2004. Rapid population decline in red knots: fitness consequences of decreased refuelling rates and late arrival in Delaware Bay. Proc. R. Soc. Lond. Ser. B Biol. Sci. 271, 875–882.

Battjes, J.A., Janssen, J., 1978. Energy loss and set-up due to breaking of random waves, 1978 Coast. Eng. 569–587.

Bayraktarov, E., Saunders, M.I., Abdullah, S., Mills, M., Beher, J., Possingham, H.P., Mumby, P.J., Lovelock, C.E., 2016. The cost and feasibility of marine coastal restoration. Ecol. Appl. 26, 1055–1074.

Bento, P.M.R., Pombo, J.A.N., Mendes, R.P.G., Calado, M.R.A., Mariano, S., 2021. Ocean wave energy forecasting using optimised deep learning neural networks. Ocean Eng. 219, 108372.

Besse, G., Sakib, S., Gang, D., Hayes, D., 2018. Performance characterization of a novel marsh shoreline protection technology: the Wave Suppression and Sediment Collection (WSSC) system. Ocean Eng. 154, 216–225.

Booij, N., Ris, R.C., Holthuijsen, L.H., 1999. A third-generation wave model for coastal regions: 1. Model description and validation. J. Geophys. Res. Ocean. 104, 7649–7666.

Carniello, L., D'Alpaos, A., Defina, A., 2011. Modeling wind waves and tidal flows in shallow micro-tidal basins. Estuar. Coast Shelf Sci. 92, 263–276.

Chen, J.-L., Ralston, D.K., Geyer, W.R., Sommerfield, C.K., Chant, R.J., 2018. Wave generation, dissipation, and disequilibrium in an embayment with complex bathymetry. J. Geophys. Res. Ocean. 123, 7856–7876.

Chen, Q., Kirby, J.T., Dalrymple, R.A., Kennedy, A.B., Chawla, A., 2000. Boussinesq modeling of wave transformation, breaking, and runup. II: 2D. J. Waterw. Port Coast. Ocean Eng. 126, 48–56. https://doi.org/10.1061/(ASCE)0733-950X (2000) 126:1(48).

Chen, Z., Liu, Y., Sun, H., 2021. Physics-informed learning of governing equations from scarce data. Nat. Commun. 12, 1–13.

Cornejo-Bueno, L., Nieto-Borge, J.C., García-Díaz, P., Rodríguez, G., Salcedo-Sanz, S., 2016. Significant wave height and energy flux prediction for marine energy applications: a grouping genetic algorithm - extreme Learning Machine approach. Renew. Energy 97. https://doi.org/10.1016/j.renene.2016.05.094.

Deo, M.C., Jha, A., Chaphekar, A.S., Ravikant, K., 2001. Neural networks for wave forecasting. Ocean Eng. 28 https://doi.org/10.1016/S0029-8018(00)00027-5.

Deo, M.C., Naidu, C.S., 1998. Real time wave forecasting using neural networks. Ocean Eng. 26, 191–203.

Elbisy, M.S., Elbisy, A.M.S., 2021. Prediction of significant wave height by artificial neural networks and multiple additive regression trees. Ocean Eng. 230, 109077.

Everett, T., Chen, Q., Karimpour, A., Twilley, R., 2019. Quantification of swell energy and its impact on wetlands in a Deltaic estuary. Estuar. Coast 42. https://doi.org/10.1007/s12237-018-0454-z.

Glorot, X., Bengio, Y., 2010. Understanding the difficulty of training deep feedforward neural networks. In: Proceedings of the Thirteenth International Conference on Artificial Intelligence and Statistics, pp. 249–256.

Hwang, P.A., Ocampo-Torres, F.J., García-Nava, H., 2012. Wind sea and swell separation of 1D wave spectrum by a spectrum integration method. J. Atmos. Ocean. Technol. 29 https://doi.org/10.1175/JTECH-D-11-00075.1.

James, S.C., Zhang, Y., O'Donncha, F., 2018. A machine learning framework to forecast wave conditions. Coast. Eng. 137 https://doi.org/10.1016/j.coastaleng.2018.03.004.

Jörges, C., Berkenbrink, C., Stumpe, B., 2021. Prediction and reconstruction of ocean wave heights based on bathymetric data using LSTM neural networks. Ocean Eng. 232, 109046.

Karimpour, A., Chen, Q., 2017. Wind wave analysis in depth limited water using OCEANLYZ, A MATLAB toolbox. Comput. Geosci. 106 https://doi.org/10.1016/j.cageo.2017.06.010.

Karimpour, A., Chen, Q., 2016. A simplified parametric model for fetch-limited peak wave frequency in shallow estuaries. J. Coast Res. 32 https://doi.org/10.2112/JCOASTRES-D-15-00145.1.

Karimpour, A., Chen, Q., Twilley, R.R., 2017. Wind wave behavior in fetch and depth limited estuaries. Sci. Rep. 7, 40654.

Kingma, D.P., Ba, J., 2014. Adam: a method for stochastic optimization. arXiv Prepr. arXiv1412.6980.

Kissas, G., Yang, Y., Hwuang, E., Witschey, W.R., Detre, J.A., Perdikaris, P., 2020. Machine learning in cardiovascular flows modeling: predicting arterial blood pressure from non-invasive 4D flow MRI data using physics-informed neural networks. Comput. Methods Appl. Mech. Eng. 358, 112623.

Kopp, R.E., Horton, R.M., Little, C.M., Mitrovica, J.X., Oppenheimer, M., Rasmussen, D. J., Strauss, B.H., Tebaldi, C., 2014. Probabilistic 21st and 22nd century sea-level projections at a global network of tide-gauge sites. Earth's Future 2, 383–406.

Kukulka, T., Jenkins III, R.L., Kirby, J.T., Shi, F., Scarborough, R.W., 2017. Surface wave dynamics in Delaware Bay and its adjacent coastal shelf. J. Geophys. Res. Ocean. 122, 8683–8706.

Lee, J.-W., Irish, J.L., Bensi, M.T., Marcy, D.C., 2021. Rapid prediction of peak storm surge from tropical cyclone track time series using machine learning. Coast. Eng. 170, 104024.

Makarynskyy, O., 2006. Neural pattern recognition and prediction for wind wave data assimilation. Pac Ocean 3, 76–85.

Malekmohamadi, I., Bazargan-Lari, M.R., Kerachian, R., Nikoo, M.R., Fallahnia, M., 2011. Evaluating the efficacy of SVMs, BNs, ANNs and ANFIS in wave height prediction. Ocean Eng. 38 https://doi.org/10.1016/j.oceaneng.2010.11.020.

Mares-Nasarre, P., Molines, J., Gómez-Mart\'\in, M.E., Medina, J.R., 2021. Explicit Neural Network-derived formula for overtopping flow on mound breakwaters in depth-limited breaking wave conditions. Coast. Eng. 164, 103810.

Mariotti, G., Fagherazzi, S., Wiberg, P.L., McGlathery, K.J., Carniello, L., Defina, A., 2010. Influence of storm surges and sea level on shallow tidal basin erosive processes. J. Geophys. Res. Ocean. 115.

Mariotti, G., Huang, H., Xue, Z., Li, B., Justic, D., Zang, Z., 2018. Biased wind measurements in estuarine waters. J. Geophys. Res. Ocean. 123, 3577–3587.

McLoughlin, S.M., Wiberg, P.L., Safak, I., McGlathery, K.J., 2015. Rates and forcing of marsh edge erosion in a shallow coastal bay. Estuar. Coast 38, 620–638.

Miky, Y., Kaloop, M.R., Elnabwy, M.T., Baik, A., Alshouny, A., 2021. A Recurrent-Cascade-Neural network-nonlinear autoregressive networks with exogenous inputs (NARX) approach for long-term time-series prediction of wave height based on wave characteristics measurements. Ocean Eng. 240, 109958.

Oh, J., Suh, K.-D., 2018. Real-time forecasting of wave heights using EOF–wavelet–neural network hybrid model. Ocean Eng. 150, 48–59.

Pareja-Roman, L.F., Chant, R.J., Ralston, D.K., 2019. Effects of locally generated wind waves on the momentum budget and subtidal exchange in a coastal plain estuary. J. Geophys. Res. Ocean. 124, 1005–1028.

Parker, K., Hill, D.F., 2017. Evaluation of bias correction methods for wave modeling output. Ocean Model. 110, 52–65.

Pirhooshyaran, M., Snyder, L.V., 2020. Forecasting, hindcasting and feature selection of ocean waves via recurrent and sequence-to-sequence networks. Ocean Eng. 207, 107424.

Priestas, A.M., Mariotti, G., Leonardi, N., Fagherazzi, S., 2015. Coupled wave energy and erosion dynamics along a salt marsh boundary, Hog Island Bay, Virginia, USA. J. Mar. Sci. Eng. 3, 1041–1065.

Sadeghifar, T., Nouri Motlagh, M., Torabi Azad, M., Mohammad Mahdizadeh, M., 2017. Coastal wave height prediction using recurrent neural networks (RNNs) in the south caspian sea. Mar. Geodes. 40 https://doi.org/10.1080/01490419.2017.1359220.

Salatin, R., Chen, Q., Bak, A.S., Shi, F., Brandt, S.R., 2021. Effects of wave coherence on longshore variability of nearshore wave processes. J. Geophys. Res. Ocean. 126, e2021JC017641.

Sanford, L.P., Gao, J., 2018. Influences of wave climate and sea level on shoreline erosion rates in the Maryland Chesapeake Bay. Estuar. Coast 41, 19–37.

Schwimmer, R.A., 2001. Rates and processes of marsh shoreline erosion in Rehoboth Bay, Delaware, USA. J. Coast Res. 672–683.

Shchepetkin, A.F., McWilliams, J.C., 2005. The regional oceanic modeling system (ROMS): a split-explicit, free-surface, topography-following-coordinate oceanic model. Ocean Model. 9, 347–404.

Smith, C., Rudd, M., Gittman, R.K., Melvin, E., Patterson, V., Renzi, J., Wellman, E., Silliman, B., 2020. Coming to terms with living shorelines: a scoping review of novel restoration strategies for shoreline protection. Front. Mar. Sci. 7, 434.

Stringari, C.E., Harris, D.L., Power, H.E., 2019. A novel machine learning algorithm for tracking remotely sensed waves in the surf zone. Coast. Eng. 147, 149–158.

Tolman, H.L., 1991. A third-generation model for wind waves on slowly varying, unsteady, and inhomogeneous depths and currents. J. Phys. Oceanogr. 21 https://doi.org/10.1175/1520-0485(1991)021<0782:atgmfw>2.0.co, 2.

Wang, H., Capurso, W.D., Chen, Q., Zhu, L., Niemoczynski, L., Snedden, G., 2021. Assessment of Wave Attenuation, Current Patterns, and Sediment Deposition and Erosion during Winter Storms by Living Shoreline Structures in Gandys Beach, New Jersey. No. 2021-1040. US Geological Survey.

Wang, H., Zhu, L., Chen, Q., Capurso, W.D., Niemoczynski, L.M., Hu, K., Snedden, G., 2020. Field Observations and Spectral Evolution of Wind Waves in Upper Delaware Bay with Living Shorelines. U.S. Geological Survey data release. https://doi.org/10.5066/P9YEUNTM.

Wang, N., Chen, Q., Zhu, L., Sun, H., 2022. Integration of data-driven and physics-based modeling of wind waves in a shallow estuary. Ocean Model. 101978. https://doi.org/10.1016/j.ocemod.2022.101978.

Wei, Z., 2021. Forecasting wind waves in the US Atlantic Coast using an artificial neural network model: towards an AI-based storm forecast system. Ocean Eng. 237, 109646.

Wei, Z., Davison, A., 2022. A convolutional neural network based model to predict nearshore waves and hydrodynamics. Coast. Eng. 171, 104044.

Wiberg, P.L., Taube, S.R., Ferguson, A.E., Kremer, M.R., Reidenbach, M.A., 2019. Wave attenuation by oyster reefs in shallow coastal bays. Estuar. Coast 42, 331–347.

Willard, J., Jia, X., Xu, S., Steinbach, M., Kumar, V., 2020. Integrating physics-based modeling with machine learning: a survey. arXiv Prepr. arXiv2003.04919.

Zheng, Z., Ma, X., Ma, Y., Dong, G., 2020. Wave estimation within a port using a fully nonlinear Boussinesq wave model and artificial neural networks. Ocean Eng. 216, 108073.

Zhu, L., Chen, Q., Wang, H., Capurso, W., Niemoczynski, L., Hu, K., Snedden, G., 2020. Field observations of wind waves in upper Delaware bay with living shorelines. Estuar. Coast 1–17.